

# Field emission from AlGa<sub>N</sub> nanowires with low turn-on field

Filippo Giubileo <sup>\*,a</sup>, Antonio Di Bartolomeo <sup>\*,b,a</sup>, Yun Zhong <sup>c</sup>, Songrui Zhao <sup>c</sup>,  
Maurizio Passacantando <sup>d</sup>

<sup>a</sup> CNR-SPIN Salerno, via Giovanni Paolo II n. 132, Fisciano 84084, Italy.

<sup>b</sup> Physics Department, University of Salerno, via Giovanni Paolo II n. 132, Fisciano 84084, Italy.

<sup>c</sup> Department of Electrical and Computer Engineering, McGill University, 3480 University Street, Montreal, Quebec H3A 0E9, Canada

<sup>d</sup> Department of Physical and Chemical Science, University of L'Aquila, and CNR-SPIN L'Aquila, via Vetoio, Coppito 67100, L'Aquila, Italy.

E-mail: filippo.giubileo@spin.cnr.it (Filippo Giubileo) and adibartolomeo@unisa.it (Antonio Di Bartolomeo).

## Abstract

We fabricate AlGa<sub>N</sub> nanowires by molecular beam epitaxy and we investigate their field emission properties by means of an experimental setup using nano-manipulated tungsten tips as electrodes, inside a scanning electron microscope. The tip-shaped anode gives access to local properties, and allows collecting electrons emitted from areas as small as  $1\mu\text{m}^2$ . The field emission characteristics are analysed in the framework of Fowler-Nordheim theory and we find a field enhancement factor as high as  $\beta = 556$  and a minimum turn-on field  $E_{\text{turn-on}} = 17\text{ V}/\mu\text{m}$  for a cathode-anode separation distance  $d = 500\text{ nm}$ . We show that for increasing separation distance,  $E_{\text{turn-on}}$  increases up to about  $35\text{ V}/\mu\text{m}$  and  $\beta$  decreases to  $\sim 100$  at  $d = 1600\text{ nm}$ . We also demonstrate the time stability of the field emission current from AlGa<sub>N</sub> nanowires for several minutes. Finally, we explain the observation of modified slope of the Fowler-Nordheim plots at low fields in terms of non-homogeneous field enhancement factors due to the presence of protruding emitters.

Keywords: aluminium gallium nitride, nanowires, field emission, field enhancement factor, emission stability

## 1. Introduction

Binary group III-Nitride semiconductors, such as GaN, AlN, and InN are important materials for optoelectronic applications, due to their direct bandgap and doping capabilities [1]. The large breakdown field, the high electron mobility, and their mechanical and thermal robustness, make them optimal candidates also for high power electronics [2]. In the last two decades, one-dimensional (1D) III-V semiconductor nanowires (NWs) have attracted great

attention due to several unique physical, electrical and optical properties [3] that can be exploited for next-generation devices such as solar cells [4], light emitting diodes [5], memory devices [6], etc. In addition, ternary compounds have wide bandgap tunability depending on the element composition [7]. Among ternary semiconductor NWs, aluminum gallium nitride ( $\text{Al}_x\text{Ga}_{1-x}\text{N}$ ) nanowires are considered very promising for ultraviolet light-emitting diodes and lasers [8–11], due to their tunable direct bandgap (3.4 eV - 6 eV, corresponding to  $\sim 207\text{ nm} - 364\text{ nm}$ ). Moreover, AlGa<sub>N</sub> thin films and NWs

have been considered for efficient electron field emission cathodes with low threshold electric field and large emission current density [12–14]. Field emission (FE) devices are very attractive to realize controlled electron transport in vacuum [15], flat panels [16,17], high frequency electromagnetic waves amplifiers and generators [18–20], electron [21] or X-ray sources [22,23]. Electron field emission from nanostructured surfaces of GaN and AlGaIn has been reported [24] at turn-on fields of the order of 10-100 V/ $\mu\text{m}$  and explained in terms of effective work function lowering caused by electron inter-valley transition upon heating and on energy band reconstruction of the surface of the nanowires due to quantum size-confinement effect [24]. Low turn-on voltage of 2.3 V has been reported [13] for AlGaIn/GaN lateral field emission nano-void channel device in which the semiconducting emitter and the metal collector are separated by a gap of about 45 nm, corresponding to a turn-on field of about 50 V/ $\mu\text{m}$ . Nanostructured AlGaIn/GaN quantum wells have been suggested [25] as field-enhanced multilayered quantum emitters, more robust than 1D nanostructures under high current density conditions, and have been theoretically modelled considering a generalized FE mechanism in which three distinct FE modes depending on the applied field are proposed [12]. Ultrathin layers of GaN(4 nm) / Al<sub>0.5</sub>Ga<sub>0.5</sub>N (2 nm) have been used as electron emitting surface [26] reporting stable FE current densities up to  $3 \times 10^{-2}$  A/cm<sup>2</sup> with a turn-on field of about 50 V/ $\mu\text{m}$ . In this case, a dual-barrier model with a two-step mechanism for the electron emission process is proposed [26], taking into account the space charge formation in the quantum well structure at the surface. Reproducible peaks in the field emission characteristics have been reported [27] for photoelectrochemically etched Al<sub>0.3</sub>Ga<sub>0.7</sub>N/GaN heterostructures and interpreted as resonant tunnelling through a multibarrier structure.

In this paper, we report a comprehensive study of the field emission properties of AlGaIn nanowires, performed inside a scanning electron microscope vacuum chamber in which a nanometric tip-shaped anode enables the collection of electrons from areas as small as 1 $\mu\text{m}^2$ . We show the homogeneity of the field emission properties on large areas and we report evidence of low turn-on field (17 V/ $\mu\text{m}$ ) and high field enhancement factor (556) at very small cathode-anode separation distance (500 nm). We finally demonstrate the robustness and the stability of AlGaIn NWs as field emitters and their suitability for large area cold cathodes.

## 2. Materials and methods

Radio-frequency (RF) plasma-assisted molecular beam epitaxy (MBE) technique was used to grow AlGaIn nanowires (NWs) on a GaN nanowire template on Si(111) substrates. Silicon solvent cleaning and hydrofluoric acid etching were

employed to clean the substrate and remove the surface oxide before loading in the MBE chamber. Then, thermal outgassing was performed at 830°C before the growth process. We notice that no patterning procedure was involved in the fabrication process. First, GaN nanowire template was grown for 30 minutes at  $T_{\text{GaN}} = 760$  °C followed by 1 hour AlGaIn growth at 785 °C obtaining a nanowire density of  $\sim 1.5 \times 10^{10}$  cm<sup>-2</sup>, overall NW length of about 300 nm and diameter of about 30-50 nm. NW density can be tuned by varying the growth temperature of the GaN template, from  $\sim 0.8 \times 10^{10}$  cm<sup>-2</sup> (for  $T_{\text{GaN}} = 775$  °C) to  $\sim 2.4 \times 10^{10}$  cm<sup>-2</sup> (for  $T_{\text{GaN}} = 745$  °C). Further fabrication details are available elsewhere [28,29]. In this study, samples with 40% Al content are investigated. In figure 1a, the top image of AlGaIn NWs by scanning electron microscope (SEM) is reported.

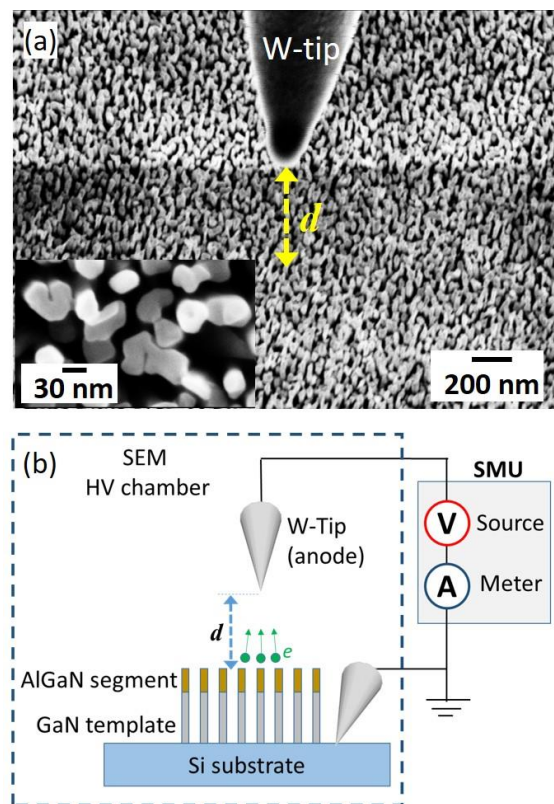


**Figure 1.** (a) SEM image of AlGaIn nanowires and tungsten tip anode approaching the surface at a distance  $d$  from the same surface. Inset: magnified image of the surface. (b) Schematic of the FE setup inside the vacuum chamber of a SEM. Nano-controlled electrodes (tungsten tips) are connected to external source-meter unit.

The crystalline structure of the sample was investigated by means of X-ray diffraction (XRD) technique, using a Bruker D5000 setup equipped with Cu  $K_{\alpha}$  (wavelength  $\lambda = 0.154$  nm) line excitation source and in Bragg-Brentano geometry, where almost all the information about the crystal structure comes from the lattice planes parallel to the substrate surface. All the

XRD spectra were acquired using a Ni filter to reduce the intensity of the  $K_{\beta}$  line in the X-ray spectrum.

X-ray photoelectron spectroscopy (XPS) has been used to analyze the surface elemental composition of the samples under investigation. Experiments have been performed by means of PHI 1257 system equipped with a hemispherical analyser (Physical Electronics Inc.), operating at pressure lower than  $10^{-9}$  mbar and using a non-monochromatic Mg  $K_{\alpha}$  source ( $h\nu = 1253.6$  eV).

The experimental setup for field emission characterization is realized inside a Zeiss LEO 1530 scanning electron microscope (SEM) working at a base pressure of about  $10^{-6}$  mbar and equipped with two piezoelectric driven nanomanipulators (MM3A by Kleindiek) to finely control (with step resolution of 5 nm) tungsten tip probes with curvature radius of about 100 nm. The metallic tips (working as in-situ electrodes) are connected to a semiconductor parameter analyzer (Keithley 4200 SCS) to perform electrical measurements by applying a bias in the range 0 – 120V and measuring the current with a resolution better than  $10^{-13}$  A. The sample under investigation and the nanomanipulators are both installed on a tilting stage inside the vacuum chamber of the microscope, allowing precise estimation of the cathode-anode separation distance for the field emission device. A layout of the experimental setup is reported in figure 1b.

### 3. Results and discussion

#### 3.1 XRD analysis

In figure 2a, we show the typical  $2\theta$  XRD pattern of AlGaIn/GaN NWs on silicon (111) substrate, comparing it with the pattern obtained for the bare silicon (111) substrate. Si (111) and its 2<sup>nd</sup> order peaks (not shown here) are resolved at  $28.4^{\circ}$  and  $58.9^{\circ}$ , respectively. Moreover, the diffraction peaks for GaN(0002),  $Al_{0.4}Ga_{0.6}N(0002)$  and Si(111), confirm the high crystallinity with the c-axis normal to Si(111). It has been shown [30] that AlGaIn layer on AlN template exhibits an XRD pattern with fixed AlN(0002) peak due to the template, while the AlGaIn peak appear at angle higher than what is expected for GaN(0002) with peak position moving towards GaN(0002) position for reducing Al content. Similarly, for AlGaIn NWs grown on GaN template on Si(111) substrate, we found the GaN(0002) peak at  $34.66^{\circ}$  and  $Al_{0.4}Ga_{0.6}N(0002)$  peak at  $35.60^{\circ}$  (between  $34.63^{\circ}$  for GaN(0002) and  $36.04^{\circ}$  AlN(0002) at which would be expected as reported in the JCPDS 065-3410 and JCPDS 025-1133, respectively). At higher angles, we also resolve GaN(0004) and  $Al_{0.4}Ga_{0.6}N(0004)$  peaks at  $73.20^{\circ}$  (in accordance with the JCPDS 065-3410) and  $75.62^{\circ}$ , respectively, while AlN(0004) would be expected at  $76.44^{\circ}$  (according to the JCPDS 025-1133). These data confirm the

high homogeneity of Al doping in the NWs, with no indications of Al segregation or pure AlN formation, and that there is no presence of cubic phase of GaN, within the detection limit of the XRD, thus it can be confirmed that the  $Al_{0.4}Ga_{0.6}N$  and GaN NWs have a hexagonal structure. As further confirmation, we show in figure 2a the comparison with the XRD pattern taken on a sample with a lower Al content ( $\sim 20\%$ ), grown with the same process. Accordingly, the GaN related peaks appear at the same angles as for 40% Al content, while the  $Al_{0.2}Ga_{0.8}N$  related peaks, due to the reduced doping, appear shifted to lower angles, closer to the GaN peaks. The peak position measured from the XRD spectra allows us to calculate the lattice constant  $c$  by using Bragg's law:  $d(hkl) = \lambda/2\sin\theta$  and  $d(hkl) = c/\sqrt{h^2 + k^2 + l^2}$ , where  $\lambda$  is the wavelength of X-ray and  $d(hkl)$  is the distance between planes given by the Miller indices ( $hkl$ ). The lattice constant  $c$  was calculated from all the symmetric reflections and the corresponding values have been listed in Table 1.

**Table 1.** Summary of the lattice constant  $c$  obtained by XRD spectra.

NWs	$2\theta^{\circ}$	$d(0002)$ ( $\text{\AA}$ )	Lattice constant $c$ ( $\text{\AA}$ )
GaN	34.66	2.586	5.172
$Al_{0.4}Ga_{0.6}N$	35.60	2.520	5.040
GaN	34.63	2.588	5.176
$Al_{0.2}Ga_{0.8}N$	35.02	2.560	5.120

#### 3.2 XPS characterization

XPS measurements are very useful to determine the chemical composition of the surface, giving information on the elements as well as their chemical state, for a thickness of about 10 nm. In figure 2b we show the survey spectrum, measured for binding energies (BE) up to 1200 eV, in which we can observe several peaks related to Ga, Al, C, N, and O. We have then calibrated all XPS spectra with respect the C 1s peak, considering that the binding energy of adventitious carbon is expected 284.8 eV [31]. Moreover, all peaks were deconvoluted, using Voigt multiplets and a Shirley background. In Figure 2c, we show the spectrum N 1s that is the result of convolution of two main component peaks centered at BE of 397.0 eV (N-Al bond) and 398.3 eV (N-Ga bond), showing a quite large area ratio of N-Al to N-Ga, in agreement with previously reported data for AlGaIn with similar or even lower Al content [32,33], probably due to a slightly excess of Al content in the top most surface layer. In Figure 2d, we show the Al 2p spectrum that can be reproduced by two component peaks corresponding to Al-N bonds at a BE= 73.4 eV and Al-O bonds at 74.5 eV, the area ratio Al-O/Al-N being about 0.17.

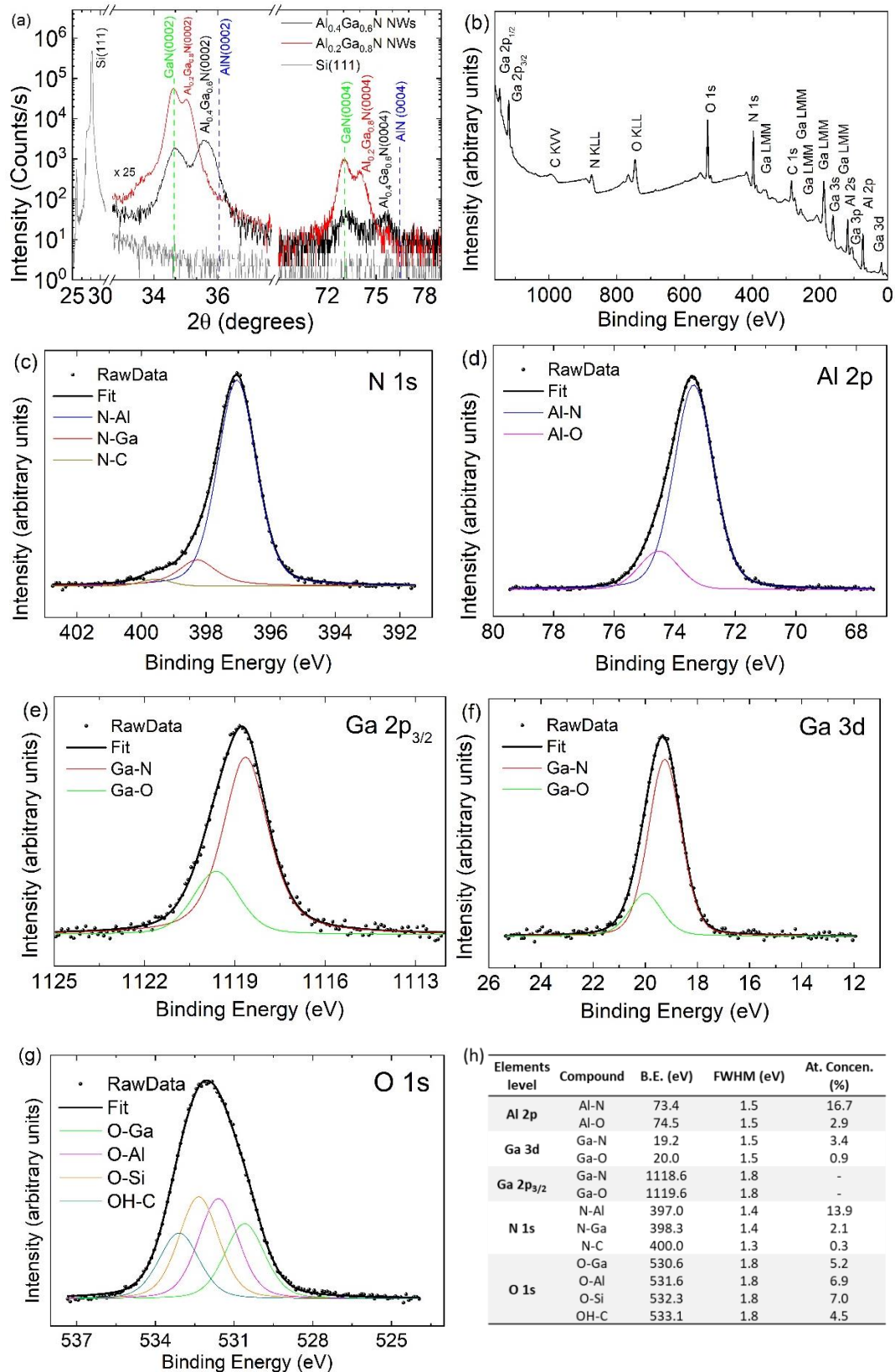


**Figure 2.** XRD and XPS characterization of AlGaIn nanowires. (a) XRD pattern, measured for  $\text{Al}_{0.4}\text{Ga}_{0.6}\text{N}$  nanowires grown on GaN template on Si (111), is compared to XRD pattern of the  $\text{Al}_{0.2}\text{Ga}_{0.8}\text{N}$  nanowires and of the Si (111) substrate. (b) XPS characterization, survey spectrum; deconvoluted XPS spectra of (c) N 1s, (d) Al 2p, (e) Ga 2p<sub>3/2</sub>, (f) Ga 3d, (g) O 1s. (h) Summary of XPS data: BE, FWHM and atomic concentration.

Ga  $2p_{3/2}$  spectrum is deconvoluted in Figure 2e, evidencing the presence of two component peaks, namely the Ga-N bonds at 1118.6 eV and the Ga-O bonds at 1119.6 eV [33]. Finally, Ga 3d spectrum is deconvoluted (Figure 2f) in two component peaks as well, the Ga-N bonds at 19.2 eV and the Ga-O bonds at 20.0 eV, with an area ratio Ga-O/Ga-N of about 0.26. The signal due to Ga-O bonds (and to Al-O bonds) indicates the presence of a thin oxide layer on the surface, which is probably amorphous, not being evidenced by the XRD pattern. We notice that a thin oxide layer (of the order of 1 nm) does not significantly affect the FE behavior of the NWs, the only effect being to introduce a small extra tunnel barrier to overcome, corresponding to a slightly increase of the turn-on field with respect of an oxide-free surface.

In figure 2g, we also show the deconvolution of the O 1s spectrum, identifying four component peaks, namely the O-Ga bonds at 530.6 eV, the O-Al bonds at 531.6 eV, the O-Si bonds at 532.3 eV and the OH-C bonds at 533.1 eV.

In figure 2h we summarize the BE, the Full Width at Half Maximum (FWHM) and the atomic concentration for the deconvoluted XPS spectra.

### 3.3 Field emission

To perform field emission characterization, we started by approaching both nano-manipulated probes on the sample surface. Once the electrical contact was established, the tungsten tip used as the anode was gently detached and positioned at controlled distance from the surface, thus obtaining the circuit configuration for FE measurements (schematic is shown in figure 1b). The piezoelectric control of the tungsten tips allows precise tuning of the cathode-anode separation distance  $d$  with 5 nm spatial resolution. In figure 3a we show the current-voltage ( $I - V$ ) characteristics, measured by applying an external bias sweep up to +100V on the tip anode, to collect electrons field emitted from the AlGaIn nanowires, for different cathode-anode separation distances, in the range 500 nm – 1400 nm. Larger bias was avoided to prevent discharge failure, emitters burning and/or damages to the nano-manipulator circuitry. In order to verify the robustness of the FE device as well as to check the repeatability of the measurements, we standardly performed at least two successive I-V sweeps; this allowed us to exclude effects and/or modifications induced by electrical stress. Similarly, we repeatedly performed SEM imaging of the emitting area under investigation, before and after I-V measurements, to further confirm the surface stability.

In figure 3b, experimental data are plotted on logarithmic scale in order to better visualize the current rising. Indeed, for  $d = 500$  nm, we observe a turn-on voltage (here defined as the voltage necessary to get a current of 1 pA)  $V_{on} = 15$ V. Then,

the current exponentially grows for about six orders of magnitude up to the  $\mu$ A. Similarly, at  $d = 1100$ nm the FE current starts at  $V_{on} = 38$ V and at  $d = 1400$ nm the FE current starts at  $V_{on} = 52$ V. To analyse the I-V curves, we compare experimental data with the expected behaviour (solid lines in figure 3b) in the framework of Fowler-Nordheim (FN) theory [34]. According to this model, the emitted current from a planar metallic surface can be expressed in the form:

$$I = S \cdot A \phi^{-1} \left( \beta \frac{V}{d} \right)^2 \exp \left[ -B \phi^{3/2} \left( \beta \frac{V}{d} \right)^{-1} \right] \quad (1)$$

where  $S$  is the effective area from which electrons are field emitted,  $A = 1.54 \times 10^{-6} AV^{-2} eV$  and  $B = 6.83 \times 10^9 eV^{-3/2} m^{-1} V$  are dimensional constants,  $\phi = 4.93$  eV [35] is the work function;  $V/d = E$  is the electric field due to the applied voltage  $V$  when the anode-cathode separation distance is  $d$ , while  $\beta$  represents the field enhancement factor that originates the amplification of local electric field  $E_L$  in proximity of curved surface or apex ( $E_L = \beta V/d$ ). Accordingly, the  $\ln(I/V^2)$  versus  $1/V$  (the so-called FN plot) is expected to be a linear function, and from the slope  $m$ , one can calculate the field enhancement factor as  $\beta = -B d \phi^{3/2} m^{-1}$ . We remind here that equation (1) has been derived for standard parallel plate configuration [36] in which a planar anode is faced to a metallic and planar emitting surface.

However, despite such FN theory has been developed for emission from flat metallic surface under a uniform macroscopic electric field, it is widely accepted that it can be used as first approximation to identify the field emission nature of current collected from nanostructured surfaces, in presence of non-uniform electric field. Indeed, FN theory has been successfully applied to analyse FE from nanoparticles [37–40], semiconducting nanostructures [41], nanowires [42–46], nanotubes [47–54], two-dimensional nanosheets, such as graphene [55–58] and transition metal dichalcogenides [59–68]. For the sake of completeness, we mention here that corrections have been discussed in the literature [69–74] to include effects due to curved surfaces, series resistance, non-homogeneous field enhancement factor or work-functions, one-dimensional and two-dimensional nanostructures, semiconducting emitters, electronic structure of emitters, etc. [70–72,75]

In the following, for a more precise data analysis we need to take into account that in our setup we are employing a tip-shaped anode with a small curvature radius of about 100 nm. It has already been demonstrated that in such configuration, the field emission current collected at the anode comes from a limited circular area having diameter of the order of the cathode-anode separation distance. [76] Moreover, the anode geometry modifies the distribution of the electric field lines and the effects on the  $I - V$  characteristics can be easily modelled by introducing a correction factor  $k_{tip} \approx 1.6$  that takes into account the anode geometry, [76] so that  $\beta =$

$-Bk_{tip}d\phi^{3/2}m^{-1}$ . Moreover, the use of a tip-shaped anode allows to collect field emitted electrons from limited sample areas as small as  $\sim 1\mu\text{m}^2$  and thus to obtain local information

on the FE properties [76], in comparison to the standard parallel plate setup that provides information on areas up to  $\text{mm}^2$ .

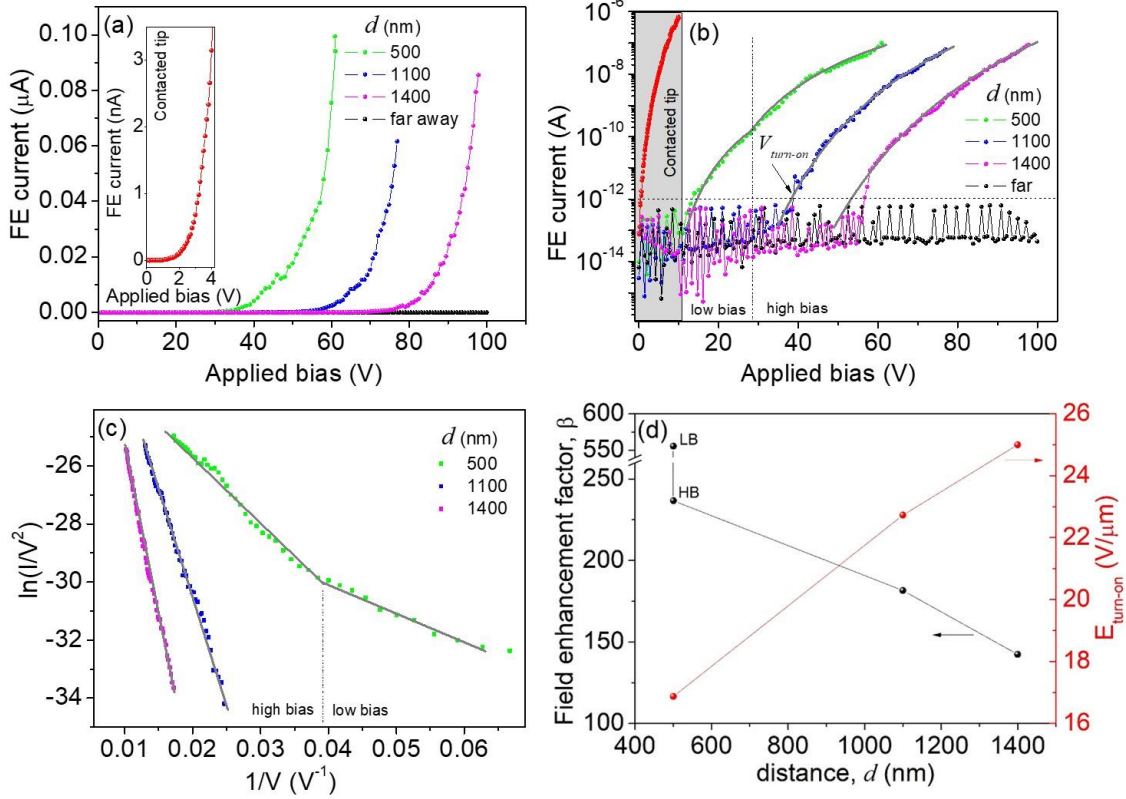


**Figure 3.** (a) Field emission  $I$ - $V$  characteristics for various cathode-anode separation distances plotted on linear scale. Inset shows the curve when anode tip is in contact with the sample surface. (b)  $I$ - $V$  characteristics plotted on semi-logarithmic scale are compared to numerically calculated curves obtained according to Fowler-Nordheim model (Equation 1). Horizontal dotted line evidences  $1\text{pA}$  level. (c) FN-plots corresponding to the  $I$ - $V$  curves and linear fittings (solid lines). (d) Field enhancement factor  $\beta$  and turn-on field  $E_{\text{turn-on}}$  as a function of the cathode-anode separation distance  $d$ . For  $d = 500\text{ nm}$ , both  $\beta$  values, for low bias (LB) and high bias (HB), are reported.

In figure 3c, we show the FN plots corresponding to the experimental data of figure 3b. Solid lines represent the linear fittings. The linearity of the FN plot demonstrates that the measured  $I$ - $V$  curves are governed by the conventional FN tunneling. Thus, we can estimate the field enhancement factor for each value of the cathode-anode separation distance, by using the slope of the FN plot obtained from the numerical fitting. We notice that the field enhancement factor results to be a decreasing function of  $d$  in the investigated range  $500\text{ nm} < d < 1400\text{ nm}$  (see figure 3d), the lowest value being  $\beta = 142$  for  $d = 1400\text{ nm}$ . For the minimal separation distance,  $d = 500\text{ nm}$ , we observe that the FN-plot is characterized by two different slopes,  $m_H = -252$  corresponding to a field enhancement factor  $\beta = 237$  for the high bias region ( $V > 30\text{ V}$ ) and  $m_L = -107$  corresponding to a field enhancement factor  $\beta = 556$  for the low bias region ( $V < 30\text{ V}$ ). Similarly, we plot in figure 2d the dependence of turn-on field  $E_{\text{turn-on}}$  (here defined as the electric field necessary to obtain a FE

current of  $1\text{pA}$ ) on the separation distance  $d$  and we observe that it is an increasing function, from a minimal value  $E_{\text{turn-on}} \approx 17\text{ V}/\mu\text{m}$  at  $d = 500\text{ nm}$  to a maximum value  $E_{\text{turn-on}} \approx 25\text{ V}/\mu\text{m}$  at  $d = 1400\text{ nm}$ . We notice here that the tip-shaped anode also affect the calculation of the turn-on field, indeed  $E_{\text{turn-on}} = k_{\text{tip}}^{-1}V_{\text{on}}/d$  [76].

The FE characterization has been repeatedly performed in several different locations of the sample surface, in order to verify the homogeneity of FE properties, and the suitability of the samples for large area applications. We show, as comparison, in figure 4, the experimental data obtained in another location. The  $I$ - $V$  curves have been measured for several separation distances in the range  $500\text{ nm} < d < 1600\text{ nm}$  (figure 4a). Once again, the FE current is a fast increasing function of the externally applied voltage and it is well described by the FN theory, as confirmed by the linear FN plots reported in figure 4b. From the slope of the linear

fittings, we can calculate the field enhancement factor for the various separation distances in this new location.

We have found that for the minimum separation  $d = 500$  nm, a double slope in the FN-plot is observed and we estimate a field enhancement factor  $\beta = 570$  for the low bias region and  $\beta = 225$  for the high bias region, with  $E_{\text{turn-on}} \approx 18$

V/ $\mu\text{m}$ . Similarly, for the maximum separation  $d = 1600$  nm, we obtain  $\beta = 105$  and  $E_{\text{turn-on}} \approx 34$  V/ $\mu\text{m}$ . The data are then compared to the values reported for the first location in figure 4c. Interestingly, we observe very similar behaviour for  $\beta$  vs  $d$  (decreasing) and  $E_{\text{turn-on}}$  vs  $d$  (increasing).

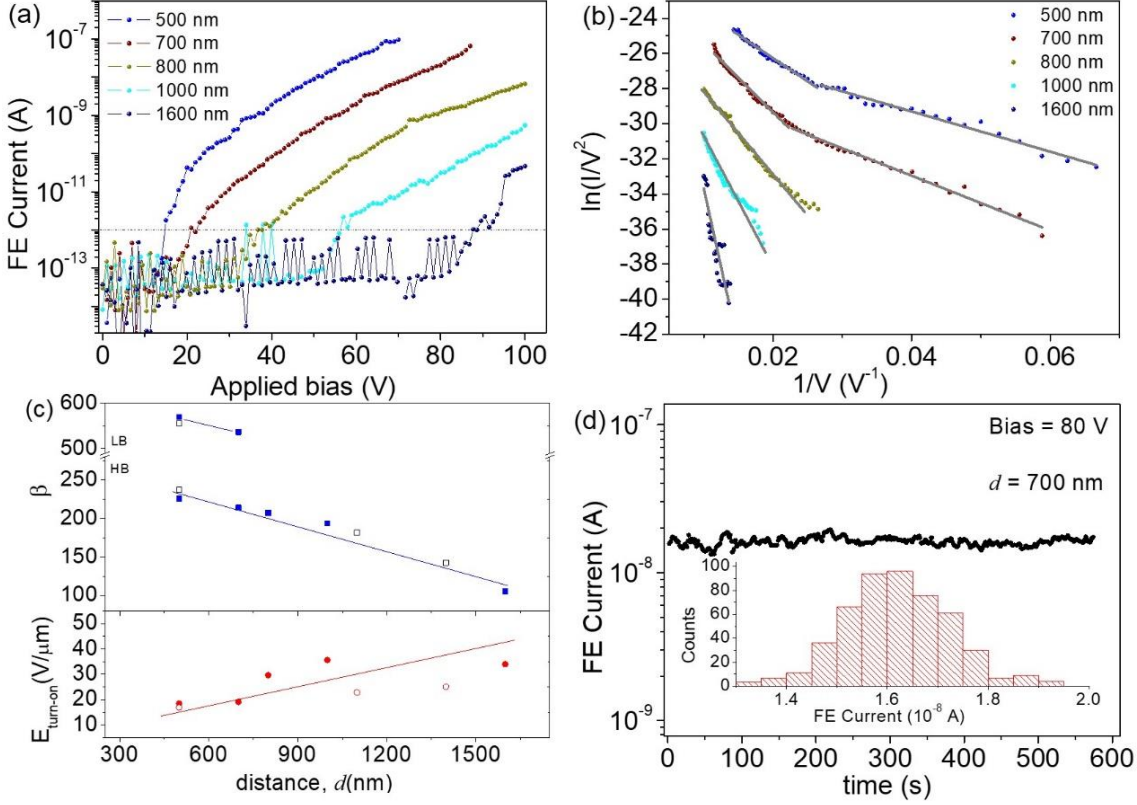


**Figure 4.** (a) Field emission I-V characteristics measured in a different location of the sample surface. Horizontal dotted line evidences 1pA level. (b) FN-plots corresponding to the I-V curves. (c) Field enhancement factor  $\beta$  (upper plot) and turn-on field  $E_{\text{turn-on}}$  (lower plot) as a function of the cathode-anode separation distance  $d$  (full symbols) are compared to previously reported values (empty symbols). Solid lines are guides for eyes. (d) Current stability (FE current versus time) measured at a cathode-anode separation distance  $d=700\text{nm}$  and at a constant bias of 80 V. The inset represents the histogram obtained from the statistical analysis of the recorded current values.

The time stability of the FE current is another crucial characteristic of a good emitter, together with the turn-on field and the field enhancement factor. Consequently, we measured the FE current versus time by keeping a fixed bias on the tip anode. We performed the experiment positioning the anode at  $d = 700$  nm from the sample surface and by applying a bias of 80 V. Experimental results are reported in figure 4d. We observe a stable current over several minutes without any significant current degradation. Moreover, from a statistical analysis of the current values (see inset of figure 4d) we notice that current fluctuations (around the average value of  $1.6 \cdot 10^{-8}$  A) are as small as 1nA (standard deviation).

We notice that in both locations, I-V characteristics show a change of slope in the FN plot, when FE is starting already at low bias. More precisely, in figure 3b we observed that the curve measured at  $d= 500$  nm has a low turn-on voltage of 17 V and the numerical simulation (according to FN theory) needs to use different parameters for low bias (LB<30V) and for high bias (HB>30V). It is not possible to reproduce experimental data with unique curve modelled by equation (1). However, in both regions the I-V curves follow separately the expected behaviour in the FN model. This is observed also in the FN plot of figure 3c, where we clearly see the change of slope in the linear behaviour. Similarly, the change of slope in the FN plots have been found for curves measured in different sample locations, as reported for example in figure 4b. To

explain the existence of two different emission regimes, one at low bias corresponding to a larger field enhancement factor, and one at high bias corresponding to a reduced field enhancement factor, we need to take into account that we are in presence of a large number of emitters that are not identical. In particular, the different heights (as observed by SEM imaging) will originate emitters with different enhancement factor. Consequently, at low applied voltages, only protruding emitters (i.e. with larger  $\beta$ ) will contribute to the emitted current, originating the first part of the I-V characteristic with a fast raising branch. For larger applied voltages, also emitters with reduced  $\beta$  will start the emission process. Consequently, at high bias, the contribution to the FE current will be due to

both kind of emitters, and the average behaviour will correspond to a lower field enhancement and thus to an increased slope of the FN plot as reported in our experimental data. A similar behaviour, with deviation of FN plots from the linearity, has been reported for graphitic nanocones [77]. Also in that case, experimental results and numerical calculations demonstrated that such behaviour was originated from the non-uniform field enhancement factors of the emitters. At low field, electrons were emitted mainly from nanocones with large  $\beta$  (corresponding to the FN plot with small slope), while at strong field, nanocones with small  $\beta$  also started to emit, reducing the average  $\beta$  (corresponding to an increased slope of the FN plot).

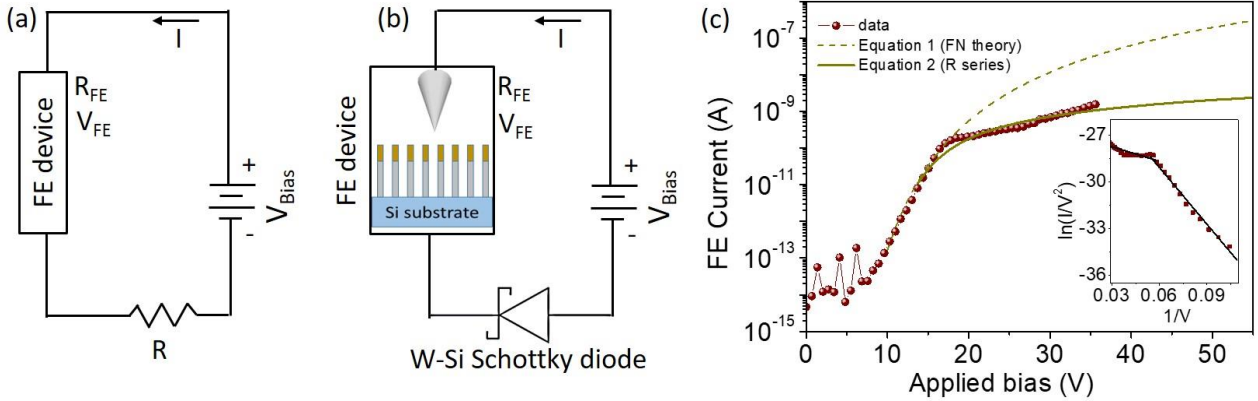


**Figure 5.** (a) Schematic of the FE circuit including a series resistance  $R$ . (b) Schematic of our FE setup with Schottky diode formed at the W-Si contact. (c) FE  $I - V$  characteristic measured after realizing a bed contact between the tip cathode and the sample in order to produce high contact resistance in series with the FE device. Experimental data are compared to FN theory (equation 1) and to the model (equation 2) that includes the presence of the series resistance  $R$ . Inset: FN plot.

In some cases, it has been found that the change of slope in the FN plots could originate instead from the presence of high resistance in series in the field emission circuit [76,78]. Indeed, from the schematic of the FE measurement setup reported in figure 5a, it is easy to understand that the presence of a large resistance  $R$  in series with the FE device causes a reduction of the applied voltage  $V_{\text{Bias}}$  (due to the voltage drop on  $R$ ). As a consequence, the voltage  $V_{\text{FE}}$  applied on the FE device is  $V_{\text{FE}} = V_{\text{Bias}} - RI$ . Assuming that the resistance  $R$  is not dependent on the field, and considering the expression of the current  $I$  according to equation 1, we obtain a recursive equation that we can solve numerically, in which the applied voltage is replaced by the effective voltage,  $V - RI$ :

$$I = S \cdot A \phi^{-1} \left( \beta \frac{V - RI}{d} \right)^2 \exp \left[ -B \phi^{3/2} \left( \beta \frac{V - RI}{d} \right)^{-1} \right] \quad (2)$$

In our setup, a second tungsten tip is used as cathode to contact the silicon substrate. We typically obtained ohmic contact that did not affect the field emission device, as shown in our experimental data reported above. On the other hand, in few cases, the tip pressure on the semiconducting surface caused the formation of a Schottky contact (see figure 5b).

Indeed, a metallic (M) tip pressed on a semiconducting (S) surface forms a MS point contact, in which a Schottky barrier can be formed at the interface. In this case, the MS contact behaves as a (Schottky) diode, and no charge carriers flux is expected through the barrier when the device is reverse biased [79,80]. During FE measurements, anode tip is positively biased, and consequently the W-Si Schottky diode results reversely biased. This causes an increase of the depletion region that would stop the current flow, unless a small leakage current. Increasing the reverse bias voltage, the current also gradually increases due to the weak barrier.

In figure 5c, we report an FE characteristic,  $I - V$ , that we measured when the W-Si contact inadvertently formed a Schottky diode. We can clearly observe that after the turn-on voltage, the FE current starts to raise according to FN theory (equation 1). However, at certain voltage, experimental data sensibly deviate from the expected FN behaviour (dashed line in figure 5c), showing limited current for voltages greater than 20 V. As already stated above, we notice that the positive biasing of the anode tip corresponds to reverse biasing of the Schottky diode. In turn, the behavior of such a diode in reverse bias can behave like a very high resistance. Consequently, we

can use equation 2 to simulate experimental data reported in figure 5c, assuming a series resistance of few  $G\Omega$  in series in the FE circuit.

Finally, we verified that FE curves reported for AlGaIn NWs and showing two slopes in the FN plots (experimental data reported in figure 3 and 4) cannot be reproduced by equation 2, in that case having an ohmic contact at the W-Si junction.

#### 4. Conclusions

The field emission properties of AlGaIn nanowires, grown by molecular beam epitaxy on GaN template on Si (111) substrate, have been investigated in detail. Piezo-driven tip-shaped anode (with curvature radius  $\sim 100$  nm) is employed to finely control its position at separation distances from the emitters of hundreds nanometres, thus allowing to collect emitted electrons from area as small as  $1\mu\text{m}^2$ . Current-voltage characteristics are analysed in the framework of Fowler-Nordheim theory, evidencing a low turn-on field of  $17\text{ V}/\mu\text{m}$  and a field enhancement factor as high as 556, at a cathode-anode separation distance of 500 nm. We explain the observation of two different slope in the F-N plots, as the existence of two different regimes, one at low fields in which only protruding emitters contribute to the FE current, a second one at higher fields in which also shorter emitters start to emit electrons, causing an average lower value of the enhancement factor.

#### References

- [1] Roul B, Kumar M, Rajpalke M K, Bhat T N and Krupanidhi S B 2015 Binary group III-nitride based heterostructures: band offsets and transport properties *J. Phys. D: Appl. Phys.* **48** 423001
- [2] Zhou C, Ghods A, Saravade V G, Patel P V, Yunghans K L, Ferguson C, Feng Y, Kucukgok B, Lu N and Ferguson I T 2017 Review—The Current and Emerging Applications of the III-Nitrides *ECS J. Solid State Sci. Technol.* **6** Q149–56
- [3] Wong-Leung J, Yang I, Li Z, Karuturi S K, Fu L, Tan H H and Jagadish C 2019 Engineering III–V Semiconductor Nanowires for Device Applications *Advanced Materials* **n/a** 1904359
- [4] Li Z, Tan H H, Jagadish C and Fu L 2018 III–V Semiconductor Single Nanowire Solar Cells: A Review *Advanced Materials Technologies* **3** 1800005
- [5] Zhao S, Lu J, Hai X and Yin X 2020 AlGaIn Nanowires for Ultraviolet Light-Emitting: Recent Progress, Challenges, and Prospects *Micromachines* **11**
- [6] Lu W and Lieber C M 2007 Nanoelectronics from the bottom up *Nature Materials* **6** 841–50
- [7] Ning C-Z, Dou L and Yang P 2017 Bandgap engineering in semiconductor alloy nanomaterials with widely tunable compositions *Nature Reviews Materials* **2** 17070
- [8] Moustakas T D and Paiella R 2017 Optoelectronic device physics and technology of nitride semiconductors from the UV to the terahertz *Rep. Prog. Phys.* **80** 106501
- [9] Le B H, Zhao S, Liu X, Woo S Y, Botton G A and Mi Z 2016 Controlled Coalescence of AlGaIn Nanowire Arrays: An Architecture for Nearly Dislocation-Free Planar Ultraviolet Photonic Device Applications *Adv. Mater.* **28** 8446–54
- [10] Yoshida H, Yamashita Y, Kuwabara M and Kan H 2008 A 342-nm ultraviolet AlGaIn multiple-quantum-well laser diode *Nature Photonics* **2** 551–4
- [11] Li X-H, Detchprohm T, Kao T-T, Satter Md M, Shen S-C, Douglas Yoder P, Dupuis R D, Wang S, Wei Y O, Xie H, Fischer A M, Ponce F A, Wernicke T, Reich C, Martens M and Kneissl M 2014 Low-threshold stimulated emission at 249 nm and 256 nm from AlGaIn-based multiple-quantum-well lasers grown on sapphire substrates *Appl. Phys. Lett.* **105** 141106
- [12] Wang R-Z, Zhao W and Yan H 2017 Generalized Mechanism of Field Emission from Nanostructured Semiconductor Film Cathodes *Sci Rep* **7** 43625
- [13] Zhao D-S, Liu R, Fu K, Yu G-H, Cai Y, Huang H-J, Wang Y-Q, Sun R-G and Zhang B-S 2018 An AI 0.25

- Ga<sub>0.75</sub>N/GaN Lateral Field Emission Device with a Nano Void Channel *Chinese Phys. Lett.* **35** 038103
- [14] Evtukh A 2015 *Vacuum nanoelectronic devices: novel electron sources and applications* (Chichester, West Sussex, United Kingdom: John Wiley & Sons, Inc)
- [15] Brodie I and Spindt C A 1992 Vacuum Microelectronics *Advances in Electronics and Electron Physics* vol 83, ed P W Hawkes (Academic Press) pp 1–106
- [16] Kim H-M, Kang T W, Chung K S, Hong J P and Choi W B 2003 Field emission displays of wide-bandgap gallium nitride nanorod arrays grown by hydride vapor phase epitaxy *Chemical Physics Letters* **377** 491–4
- [17] Talin A A, Dean K A and Jaskie J E 2001 Field emission displays: a critical review *Solid-State Electronics* **45** 963–76
- [18] Lin M-C, Huang K-H, Lu P-S, Lin P-Y and Jao R-F 2005 Field-emission based vacuum device for the generation of terahertz waves *Journal of Vacuum Science & Technology B: Microelectronics and Nanometer Structures Processing, Measurement, and Phenomena* **23** 849–52
- [19] Morev S P, Aban'shin N P, Gorfinkel' B I, Darmaev A N, Komarov D A, Makeev A E and Yakunin A N 2013 Electron-optical systems with planar field-emission cathode matrices for high-power microwave devices *Journal of Communications Technology and Electronics* **58** 357–65
- [20] Teo K B K, Minoux E, Hudanski L, Peauger F, Schnell J-P, Gangloff L, Legagneux P, Dieumegard D, Amaratunga G A J and Milne W I 2005 Carbon nanotubes as cold cathodes *Nature* **437** 968–968
- [21] Saito Y and Uemura S 2000 Field emission from carbon nanotubes and its application to electron sources *Carbon* **38** 169–82
- [22] Zhang J, Yang G, Cheng Y, Gao B, Qiu Q, Lee Y Z, Lu J P and Zhou O 2005 Stationary scanning x-ray source based on carbon nanotube field emitters *Appl. Phys. Lett.* **86** 184104
- [23] Liu Z, Yang G, Lee Y Z, Bordelon D, Lu J and Zhou O 2006 Carbon nanotube based microfocus field emission x-ray source for microcomputed tomography *Appl. Phys. Lett.* **89** 103111
- [24] Evtukh A, Yilmazoglu O, Litovchenko V, Semenenko M, Gorbanyuk T, Grygoriev A, Hartnagel H and Pavlidis D 2008 Electron field emission from nanostructured surfaces of GaN and AlGaIn *phys. stat. sol. (c)* **5** 425–30
- [25] Zhao W, Wang R-Z, Song X-M, Wang H, Wang B, Yan H and Chu P K 2011 Electron field emission enhanced by geometric and quantum effects from nanostructured AlGaIn/GaN quantum wells *Appl. Phys. Lett.* **98** 152110
- [26] Semet V, Binh V T, Zhang J P, Yang J, Khan M A and Tsu R 2004 Electron emission through a multilayer planar nanostructured solid-state field-controlled emitter *Appl. Phys. Lett.* **84** 1937–9
- [27] Semenenko M and Yilmazoglu O 2012 Specific features of field emission from an Al<sub>0.3</sub>Ga<sub>0.7</sub>N/GaN system *25th International Vacuum Nanoelectronics Conference 2012 25th International Vacuum Nanoelectronics Conference (IVNC)* (Jeju, Korea (South): IEEE) pp 1–2
- [28] Zhong Y, Berikaa E, Lu J, Yin X and Zhao S 2020 Molecular beam epitaxial growth and optical characterization of AlGaIn nanowires with reduced substrate temperature *AIP Advances* **10** 025022
- [29] Zhao S, Woo S Y, Sadaf S M, Wu Y, Pofelski A, Laleyan D A, Rashid R T, Wang Y, Botton G A and Mi Z 2016 Molecular beam epitaxy growth of Al-rich AlGaIn nanowires for deep ultraviolet optoelectronics *APL Materials* **4** 086115
- [30] Wang S, Zhang X, Dai Q, Feng Z C and Cui Y 2017 An X-ray diffraction and Raman spectroscopy investigation of AlGaIn epi-layers with high Al composition *Optik* **131** 201–6

- [31] D'Archivio A A, Maggi M A, Odoardi A, Santucci S and Passacantando M 2018 Adsorption of triazine herbicides from aqueous solution by functionalized multiwall carbon nanotubes grown on silicon substrate *Nanotechnology* **29** 065701
- [32] Jiang R and Meng X 2019 The characterization of AlGa<sub>N</sub> nanowires prepared via chemical vapor deposition *J Mater Sci: Mater Electron* **30** 16266–74
- [33] Garg M, Naik T R, Pathak R, Rao V R, Liao C-H, Li K-H, Sun H, Li X and Singh R 2018 Effect of surface passivation process for AlGa<sub>N</sub>/Ga<sub>N</sub> HEMT heterostructures using phenol functionalized-porphyrin based organic molecules *Journal of Applied Physics* **124** 195702
- [34] Fowler R H and Nordheim L 1928 Electron emission in intense electric fields *Proceedings of the Royal Society of London. Series A, Containing Papers of a Mathematical and Physical Character* **119** 173–81
- [35] Koley G and Spencer M G 2001 Surface potential measurements on Ga<sub>N</sub> and AlGa<sub>N</sub>/Ga<sub>N</sub> heterostructures by scanning Kelvin probe microscopy *Journal of Applied Physics* **90** 337–44
- [36] Giubileo F, Di Bartolomeo A, Lemmo L, Luongo G and Urban F 2018 Field Emission from Carbon Nanostructures *Applied Sciences* **8** 526
- [37] Hong X D, Liang D, Wu P Z and Zheng H R 2016 Facile synthesis and enhanced field emission properties of Cu nanoparticles decorated graphene-based emitters *Diamond and Related Materials* **69** 61–7
- [38] Lemmo L, Di Bartolomeo A, Giubileo F, Luongo G, Passacantando M, Niu G, Hatami F, Skibitzki O and Schroeder T 2017 Graphene enhanced field emission from InP nanocrystals *Nanotechnology* **28** 495705
- [39] Kumar D, Banerjee D, Sarkar S, Das N S and Chattopadhyay K K 2016 Easy synthesis of porous carbon mesospheres and its functionalization with titania nanoparticles for enhanced field emission and photocatalytic activity *Materials Chemistry and Physics* **175** 22–32
- [40] Di Bartolomeo A, Passacantando M, Niu G, Schlykow V, Lupina G, Giubileo F and Schroeder T 2016 Observation of field emission from GeSn nanoparticles epitaxially grown on silicon nanopillar arrays *Nanotechnology* **27** 485707
- [41] Fang X, Bando Y, Gautam U K, Ye C and Golberg D 2008 Inorganic semiconductor nanostructures and their field-emission applications *J. Mater. Chem.* **18** 509–22
- [42] Li Y, Zhang Z, Zhang G, Zhao L, Deng S, Xu N and Chen J 2017 Optimizing the Field Emission Properties of ZnO Nanowire Arrays by Precisely Tuning the Population Density and Application in Large-Area Gated Field Emitter Arrays *ACS Appl. Mater. Interfaces* **9** 3911–21
- [43] Giubileo F, Di Bartolomeo A, Lemmo L, Luongo G, Passacantando M, Koivusalo E, Hakkarainen T and Guina M 2017 Field Emission from Self-Catalyzed GaAs Nanowires *Nanomaterials* **7** 275
- [44] Liang Y 2019 Ge-doped ZnO nanowire arrays as cold field emitters with excellent performance *Nanotechnology* **30** 375603
- [45] Giubileo F, Passacantando M, Urban F, Grillo A, Lemmo L, Pelella A, Goosney C, LaPierre R and Di Bartolomeo A 2020 Field emission characteristics of InSb patterned nanowires *arXiv:2004.13340 [cond-mat]*
- [46] Khademi A, Azimirad R, Nien Y-T and Moshfegh A Z 2011 Field-emission enhancement of molybdenum oxide nanowires with nanoprotusions *J Nanopart Res* **13** 115–25
- [47] Sreekanth M, Ghosh S, Biswas P, Kumar S and Srivastava P 2016 Improved field emission from indium decorated multi-walled carbon nanotubes *Applied Surface Science* **383** 84–9
- [48] Giubileo F, Bartolomeo A D, Scarfato A, Lemmo L, Bobba F, Passacantando M, Santucci S and Cucolo A M 2009 Local probing of the field

- emission stability of vertically aligned multi-walled carbon nanotubes *Carbon* **47** 1074–80
- [49] Ummethala R, Wenger D, Tedde S F, Täschner C, Leonhardt A, Büchner B and Eckert J 2016 Effect of substrate material on the growth and field emission characteristics of large-area carbon nanotube forests *Journal of Applied Physics* **119** 044302
- [50] Giubileo F, Di Bartolomeo A, Sarno M, Altavilla C, Santandrea S, Ciambelli P and Cucolo A M 2012 Field emission properties of as-grown multiwalled carbon nanotube films *Carbon* **50** 163–9
- [51] Yun K N, Sun Y, Han J S, Song Y-H and Lee C J 2017 High-Performance Field-Emission Properties of Boron Nitride Nanotube Field Emitters *ACS Appl. Mater. Interfaces* **9** 1562–8
- [52] Giubileo F, Lemmo L, Luongo G, Martucciello N, Raimondo M, Guadagno L, Passacantando M, Lafdi K and Di Bartolomeo A 2017 Transport and field emission properties of buckypapers obtained from aligned carbon nanotubes *J Mater Sci* **52** 6459–68
- [53] Grillo A, Barrat J, Galazka Z, Passacantando M, Giubileo F, Lemmo L, Luongo G, Urban F, Dubourdiou C and Di Bartolomeo A 2019 High field-emission current density from  $\beta$ -Ga<sub>2</sub>O<sub>3</sub> nanopillars *Appl. Phys. Lett.* **114** 193101
- [54] Passacantando M, Bussolotti F, Santucci S, Di Bartolomeo A, Giubileo F, Lemmo L and Cucolo A M 2008 Field emission from a selected multiwall carbon nanotube *Nanotechnology* **19** 395701
- [55] Gao Y and Okada S 2019 Field emission properties of edge-functionalized graphene *Carbon* **142** 190–5
- [56] Di Bartolomeo A, Giubileo F, Lemmo L, Romeo F, Russo S, Unal S, Passacantando M, Grossi V and Cucolo A M 2016 Leakage and field emission in side-gate graphene field effect transistors *Appl. Phys. Lett.* **109** 023510
- [57] Santandrea S, Giubileo F, Grossi V, Santucci S, Passacantando M, Schroeder T, Lupina G and Di Bartolomeo A 2011 Field emission from single and few-layer graphene flakes *Appl. Phys. Lett.* **98** 163109
- [58] Wang L, Jiang L, Zhang T, Gao F, Chen S and Yang W 2019 Graphene/SiC heterojunction nanoarrays: toward field emission applications with low turn-on fields and high stabilities *J. Mater. Chem. C* **7** 13748–53
- [59] Urban F, Passacantando M, Giubileo F, Lemmo L and Di Bartolomeo A 2018 Transport and Field Emission Properties of MoS<sub>2</sub> Bilayers *Nanomaterials* **8** 151
- [60] Yang T-H, Chiu K-C, Harn Y-W, Chen H-Y, Cai R-F, Shyue J-J, Lo S-C, Wu J-M and Lee Y-H 2018 Electron Field Emission of Geometrically Modulated Monolayer Semiconductors *Advanced Functional Materials* **28** 1706113
- [61] Giubileo F, Lemmo L, Passacantando M, Urban F, Luongo G, Sun L, Amato G, Enrico E and Di Bartolomeo A 2019 Effect of Electron Irradiation on the Transport and Field Emission Properties of Few-Layer MoS<sub>2</sub> Field-Effect Transistors *J. Phys. Chem. C* **123** 1454–61
- [62] Kashid R V, Late D J, Chou S S, Huang Y-K, De M, Joag D S, More M A and Dravid V P 2013 Enhanced Field-Emission Behavior of Layered MoS<sub>2</sub> Sheets *Small* **9** 2730–4
- [63] Di Bartolomeo A, Pelella A, Urban F, Grillo A, Lemmo L, Passacantando M, Liu X and Giubileo F 2020 Field Emission in Ultrathin PdSe<sub>2</sub> Back-Gated Transistors *Adv. Electron. Mater.* 2000094
- [64] Late D J, Shaikh P A, Khare R, Kashid R V, Chaudhary M, More M A and Ogale S B 2014 Pulsed Laser-Deposited MoS<sub>2</sub> Thin Films on W and Si: Field Emission and Photoresponse Studies *ACS Appl. Mater. Interfaces* **6** 15881–8
- [65] Giubileo F, Grillo A, Passacantando M, Urban F, Lemmo L, Luongo G, Pelella A, Loveridge M, Lozzi L and Di Bartolomeo A 2019 Field Emission

- Characterization of MoS<sub>2</sub> Nanoflowers  
*Nanomaterials* **9** 717
- [66] Lemmo L, Urban F, Giubileo F, Passacantando M and Di Bartolomeo A 2020 Nanotip Contacts for Electric Transport and Field Emission Characterization of Ultrathin MoS<sub>2</sub> Flakes *Nanomaterials* **10** 106
- [67] Veeramalai C P, Li F, Liu Y, Xu Z, Guo T and Kim T W 2016 Enhanced field emission properties of molybdenum disulphide few layer nanosheets synthesized by hydrothermal method *Applied Surface Science* **389** 1017–22
- [68] Di Bartolomeo A, Urban F, Passacantando M, McEvoy N, Peters L, Lemmo L, Luongo G, Romeo F and Giubileo F 2019 A WSe<sub>2</sub> vertical field emission transistor *Nanoscale* **11** 1538–48
- [69] Edgcombe C J 2005 Development of Fowler-Nordheim theory for a spherical field emitter *Phys. Rev. B* **72** 045420
- [70] Jensen K L 1999 Exchange-correlation, dipole, and image charge potentials for electron sources: Temperature and field variation of the barrier height *Journal of Applied Physics* **85** 2667–80
- [71] Han S, Lee M H and Ihm J 2002 Dynamical simulation of field emission in nanostructures *Phys. Rev. B* **65** 085405
- [72] Forbes R G 2012 Extraction of emission parameters for large-area field emitters, using a technically complete Fowler–Nordheim-type equation *Nanotechnology* **23** 095706
- [73] Urban F, Passacantando M, Giubileo F, Lemmo L, Luongo G, Grillo A and Di Bartolomeo A 2019 Two-dimensional effects in Fowler-Nordheim field emission from transition metal dichalcogenides *Journal of Physics: Conference Series* **1226** 012018
- [74] Ang Y S, Liang S-J and Ang L K 2017 Theoretical modeling of electron emission from graphene *MRS Bulletin* **42** 505–10
- [75] Edgcombe C J and Johansen A M 2003 Current-voltage characteristics of nonplanar cold field emitters *Journal of Vacuum Science & Technology B: Microelectronics and Nanometer Structures Processing, Measurement, and Phenomena* **21** 1519–23
- [76] Di Bartolomeo A, Scarfato A, Giubileo F, Bobba F, Biasiucci M, Cucolo A M, Santucci S and Passacantando M 2007 A local field emission study of partially aligned carbon-nanotubes by atomic force microscope probe *Carbon* **45** 2957–71
- [77] Lu X, Yang Q, Xiao C and Hirose A 2006 Nonlinear Fowler–Nordheim plots of the field electron emission from graphitic nanocones: influence of non-uniform field enhancement factors *J. Phys. D: Appl. Phys.* **39** 3375–9
- [78] Luginsland J W, Valfells A and Lau Y Y 1996 Effects of a series resistor on electron emission from a field emitter *Appl. Phys. Lett.* **69** 2770–2
- [79] Di Bartolomeo A, Giubileo F, Grillo A, Luongo G, Lemmo L, Urban F, Lozzi L, Capista D, Nardone M and Passacantando M 2019 Bias Tunable Photocurrent in Metal-Insulator-Semiconductor Heterostructures with Photoresponse Enhanced by Carbon Nanotubes *Nanomaterials* **9**
- [80] Di Bartolomeo A, Grillo A, Urban F, Lemmo L, Giubileo F, Luongo G, Amato G, Croin L, Sun L, Liang S-J and Ang L K 2018 Asymmetric Schottky Contacts in Bilayer MoS<sub>2</sub> Field Effect Transistors *Adv. Funct. Mater.* **28** 1800657